EJNMMI Physics

ORIGINAL RESEARCH Open Access

Quantitative capabilities of commercial CZT SPECT-CT cameras with ^{99m}Tc

Alain Seret[1*] and Claire Bernard[2]

*Correspondence:
aseret@uliege.be

[1] GIGA Institute, University of Liège, Allée du Six Août, 19, 4000 Liège, Belgium
[2] Médecine Nucléaire et Imagerie Oncologique, CHU Liège, Avenue de l'Hôpital, 1, 4000 Liège, Belgium

Abstract

Background: This study aimed to analyse the quantitative capabilities of cadmium-zinc-telluride (CZT)-based SPECT-CT cameras using ^{99m}Tc, comparable to the analysis performed a decade ago for the sodium iodide (NaI) SPECT-CT systems available on the market at that time. This survey assessed one dual-head (GE Discovery NM870 CZT) and two ring (GE Starguide, Spectrum Dynamics Veriton 200) CZT cameras, as well as a state-of-the-art NaI dual-head system (Siemens Intevo Bold) that served as reference. Attenuation and scatter correction accuracy was explored, contrast recovery for small cold and hot rods measured, as well as the quantification in a large uniform area using user-determined conversion factors. Tomography reconstruction was performed with the manufacturers' iterative algorithms that allowed for attenuation correction, scatter correction and resolution recovery.

Results: Using the NEMA NU-2 1994 dedicated phantom, attenuation and scatter corrections seemed to perform very well. Equally, the contrast recovery of cold rods seemed to be superior for the CZT systems. However, the contrast recovery for the hot rods was inferior to the NaI camera, whereas it was comparable without the scatter correction. Finally, a quantification error of less than 5% was shown to be reachable when using adequate user-determined conversion factors. For the NaI camera, all results were similar to those of the past study.

Conclusions: Without scatter correction, the CZT SPECT systems showed contrast performance similar to the NaI camera. With scatter correction, this held true for cold objects but the contrast of hot objects was not significantly improved or was degraded depending on the system considered and the object size. Quantification errors of less than 5% were achievable. It is hoped that on-going developments at both manufacturers will improve the scatter correction accuracy.

Keywords: Contrast, CZT, Quantification, Ring-shaped, SPECT, SPECT-CT

Background

For more than half a century, a large sodium iodide (NaI) crystal coupled to photomultipliers has been unrivalled as a photon detector in general-purpose gamma cameras. The new millenium saw the development of cadmium zinc telluride (CZT)-based direct detectors [1]. They first appeared commercially in small field-of-view systems such as hand-held mini gamma cameras or cardiac-dedicated systems [2]. Later, a large field-of-view gamma camera with CZT detectors came on the market [1, 2]. More recently, a

disruptive ring concept emerged with whole body (WB) and even dynamic single photon emission computed tomography (SPECT) capabilities [2–7] allowing scintigraphy to be used as positron emission tomography has been for decades.

The huge developments in data science that have characterised the first quarter of this century have meant that, increasingly, biomedical sciences need to generate quantitative data [8]. In nuclear imaging, positron emission tomography has presented this ability for a while [9, 10]. This was much less possible for conventional nuclear medicine until the appearance of SPECT-CT systems opened the door to quantification in scintigraphy [9, 11, 12]. The potential and clinical interest of quantification has been studied in bone, brain, heart, lung and thyroid [9–17], among others, which account for the vast majority of scintigraphy explorations and are mostly conducted with ^{99m}Tc-labelled radiotracers [12]. Moreover, quantification plays a key role in dosimetry evaluation for some therapeutic procedures or patient treatment follow-up [10, 12]. Quantification cannot be helpful without reliability and accuracy. This was the context of our past standardised comparative study of the quantitative performance with ^{99m}Tc of the state-of-the art SPECT-CT systems commercially available at that time [23]. Four dual-head NaI systems from three major manufacturers were involved in this study, conducted about a decade ago.

We have now extended this study to the new disruptive ring SPECT-CT using the same materials and methods. As classical NaI gamma cameras have also evolved, one such system of the latest generation has been included as well as the CZT dual-head large field-of-view SPECT-CT camera available on the market.

Methods

The latest generation NaI SPECT-CT system considered was a Symbia Intevo Bold (I) (Siemens, Erlangen, Germany) fitted with a 3/8″ crystal and LEHR collimators. The CZT dual-head SPECT-CT was a Discovery NM 870 CZT (D) (GE HealthCare, Haifa, Israel) fitted with the WEHR45 collimator. The two ring SPECT-CT were a Starguide (S) (GE HealthCare, Haifa, Israel) and a Veriton 200 (V) (Spectrum Dynamics Medical, Caesarea, Israel) both with their standard collimators. These SPECT systems were located in three different Belgian nuclear medicine departments: I and V at CHULiège, S at CHR Citadelle Liège and D at Vivalia-Hôpital de Libramont. These four imaging systems complied with the Belgian Federal Agency for Nuclear Control requirements for use in clinics where periodic quality controls of energy peak, planar uniformity, linearity and resolution and centre of rotation are mandatory.

For dual-head rotating cameras, a 25 cm radius circular orbit was used and a total of 120 (D) or 128 (I) projections were recorded over 360° in a 128*128 matrix, eventually with a zoom (I), resulting in 2.46 (D) or 2.4 (I) mm pixel size. For the ring cameras, the focus mode [11] was enabled with 4 rotations as automatically selected by the system. The phantom diameters were much smaller than the table width. Therefore, some detector heads could not come against the phantom wall. The focus mode forced the detector heads to only scan a volume of interest fixed by the user. The selected volume corresponded to the whole phantom volume with a small security margin and the focus acquisition time was set to 100%. This means that the heads were scanning this volume for 100% of the acquisition time. The same procedure is for example used for head or

ankle acquisitions. This was different from some other clinical applications were a focus with 80% of the acquisition time can be used to increase the statistics inside the volume of interest while nevertheless acquiring during the remaining 20% of time also data from the full field of view. With V, the phantoms were wrapped in thin aluminium foil to allow their detection by the positioning system that is based on capacity measurement.

Data were recorded in list-mode. The pixel size was 2.46 mm.

A symmetric 140 keV factory default photopeak energy window was always used with a full width of 15% (I, V) or 20% (D, S) as recommended by the manufacturers when scatter correction is planned. For scatter correction, the following additional factory default windows were added: 114–126 keV (D and S), 108.5–129.5 keV (I), 109–130 keV (V). A standard low dose CT scan was also systematically performed.

Phantoms

Four cylindrical phantoms filled with distilled water and ^{99m}Tc were used [23]. One was a NEMA NU2-1994 attenuation and scatter correction accuracy phantom (NEMA) of 190 mm diameter and 200 mm height and its three air, water and Teflon inserts [24]. Two others were uniform phantoms of two different sizes (diameter × height): 94 × 80 mm (L) and 200 × 300 mm (XL). The XL phantom was also used as a contrast phantom (TOM) by adding three inserts (Fig. 1): one 40 mm thick grid with square plastic elements of 22 mm side-spaced by 12 mm, one 85 mm thick plastic cylinder with seven hollow rods (4, 6, 8, 10, 13, 16, 20 mm diameter) and one element with seven 85 mm tall plastic rods (6, 8, 10, 12, 16, 20, 25 mm diameter) glued between two thin circular plastic plates. The rod axes were parallel to the cylinder axis. The axis of the largest rod was located on the cylinder axis and the axis of the six other rods were 50 mm from the phantom axis and

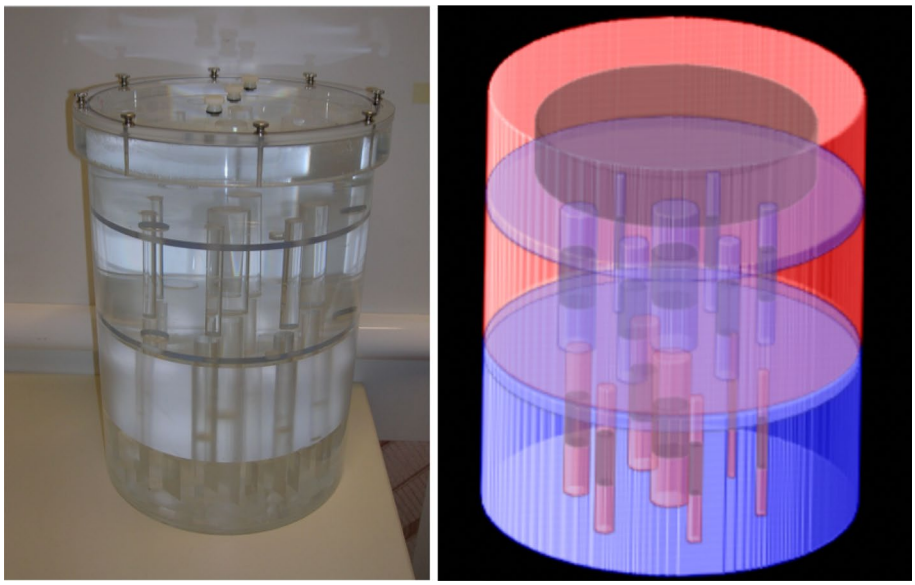

Fig. 1 Structure of TOM phantom. Left: photography. Right: 3D sketch of the three phantom parts used in this work: uniform compartment (top), cold (middle) and hot (bottom) rod inserts. Cold areas are in blue, hot areas in red and the processing ROIs (uniform and ROIF in rods) in brownish. The holes in the plates which allow a free circulation of the liquid between all compartments are not represented on the sketch but are well visible on the photography

were equally spaced angularly in the plane perpendicular to this axis. The three inserts were stacked together and left a uniform space of 65 mm height. The grid was not used further in this study, but was inserted in the phantom to keep the same experimental conditions as the past study [23] with NaI systems.

The ^{99m}Tc activity at the beginning of the acquisition was about 300 MBq in L and about 740 MBq in the three other phantoms, again following the conditions used in our past study [23]. The phantom filling was always conducted by both authors and each author had specific tasks. For each imaging system, the syringe activity was carefully measured before and after phantom injection with the radionuclide calibrators available in the department: Capintec CRC-55TR (Florham Park, NJ) for I and V, Veenstra (now Comecer) IBC Lite (Joure, The Netherlands) for D and S. The time of measurement was recorded. The radionuclide calibrators undergo daily and periodic quality controls as requested by the Belgian Federal Agency for Nuclear Control. In a national survey, these procedures have been shown to allow 5% uncertainty for ^{99m}Tc measurements [18]. The time per step of D and I was chosen in order to get [23] a total count in the main energy window of 100 Mcounts with NEMA, TOM and XL and 85 Mcounts with L in the whole set of projections. The list-mode files of S and V were rebinned in sinograms of the same total number of counts in the main energy window. Due to a filling incident, the L phantom could not be imaged with V system.

Reconstruction

The manufacturers' standard OSEM-based reconstruction algorithm (Flash3D for I, no specific name for D, S and V) was systematically used with the manufacturers' default attenuation (AC) and scatter (SC) corrections and resolution recovery (RR), unless otherwise mentioned. NEMA and TOM data were also reconstructed without scatter correction (NoSC). There was no pre- or post-filtering of the sinograms nor any noise reduction selected in the iterative reconstruction.

The number of subsets was kept at its factory default value to avoid any possible dysfunction as reported in [25]: 10 for D and S, 16 for I and V. The number of iterations was varied to span a range of updates (updates = OSEM iterations times number of subsets) from 40 (D, S) or 48 (I, V) to 240. Attenuation correction was CT-based and used the manufacturers' proprietary Hounsfield unit to attenuation coefficient conversion law. Scatter correction was performed using the dual energy window (DEW) method (D, S, V) [26] or a manufacturer-modified triple energy window (TEW) technique (I) [27, 28]. The modified version of TEW used an upper scatter window width set to zero and therefore used only one scatter window, as did DEW. Both DEW and TEW used a weighted subtraction of data recorded in the photopeak window and in the scatter window. The weight in DEW is to be defined by the operator [26] and the factory default value was used. The weight in TEW is directly computed from the energy window widths [27, 28]. Resolution recovery was performed using the manufacturers' algorithms without any modification. With V, both the so-called quantitative-oriented PSFRq and display-oriented PSFRd additional point spread function corrections were also tested. Their use is explicitly mentioned in the results. These two optional corrections are isotope specific. They were used in addition to the collimator geometrical modelling which is included in

the so-called wide beam reconstruction used by this manufacturer [19]. For quantitative purposes, a decay correction was also included [20].

Image processing

Image processing was performed using A Medical Image Data Examiner (AMIDE, version 1.0.5; Andy Loening) freeware running on a MacBook (Apple) computer. For system I, the manufacturer private DICOM tag "pixel scale factor" has been taken into account when processing the data with AMIDE.

Images of the NEMA phantom were processed as previously described [23, 24]. Eleven cylindrical (160 × 30 mm) regions of interest (ROI) were drawn: one centred per insert and eight in the background. From the mean number of counts in the insert (Ci) and in the background (Cbkg), the residual fraction (RF) in each insert was computed as RF = Ci/Cbkg. From the NoSC images, the ratio of mean counts in the background with (Cbkg_SC) and without (Cbkg_NoSC) scatter correction (RSCbkg = Cbkg_SC/Cbkg_NoSC) was computed. For the TOM phantom (Fig. 1), 30-mm tall ROI of full (ROIF) and half (ROIH) rod physical diameter were drawn and centred in the rods, as well as a large cylindrical (24 × 160 mm) and centred ROI in the uniform part. The mean number of counts in each rod ROI (Crod) and in the uniform part ROI (Cunif) was obtained. The standard deviation (SDEV) was also computed in this last ROI. The rod contrast recovery coefficient (CRC) was defined as follows: CRCcold = 1 − (Crod/Cunif) for cold rods and CRChot = Crod/Cunif for hot rods. The coefficient of variation (COV = SDEV/Cunif) of the uniform area was used as a metric of the noise level in a large uniform region [1, 23]. As the ROI size used for calibration with a uniform phantom is a subject of debate [5, 29], several cylindrical ROI were drawn in the images of the L and XL uniform phantoms. The height and diameter of these regions were equal (ROI0) to the phantom physical diameter and height, and were 2 cm or 4 cm smaller (ROI − 2, ROI − 4) or larger (ROI + 2, ROI + 4). ROI − 4 was too small and discarded for L. An additional ROI encompassing the whole reconstructed image (ROIimg) was also considered. From the ROI mean number of counts and the decay corrected activity [20] in the phantom, conversion factors (CF) were computed for each phantom and each ROI and then applied to Cbkg or Cunif to obtain a measure of the activity (Ames) in NEMA and TOM phantoms respectively. The deviation (ΔA) from the true activity (Atrue) or percent quantification error was computed as ΔA = Ames/Atrue − 1. Parameters RF, CRCcold, CRChot, COV and ΔA were expressed in percent.

Results

Most of the measured parameters changed with the increasing number of updates: a stabilisation was nevertheless observed above 190–200 updates, with the exception of the COV. For legibility of the RA and ΔA graphs, only results obtained at 192 (I, V) or 200 (D, S) updates are reported. Full results are available in Additional files 1,2,3,4,5.

RF for NEMA with and without scatter correction and RSCbkg are reported in Table 1. For V, the RF values obtained when adding PSFRq to the reconstruction were slightly lower and below the level of significance. For example, at 192 iterations and with scatter correction RF was 1.59% vs. 2.00% in air, 0.00013% vs. 0.00021% in water and 0.0019% vs. 0.0025% in Teflon. Identical RSCbkg was obtained with and without PSFRq. Increasing

Table 1 Results in the NEMA phantom with and without scatter correction

Camera	Updates	RF with scatter correction (%)			RF without scatter correction (%)			RSCbkg
		Air	Water	Teflon	Air	Water	Teflon	
D	200	2.25	1.03	< 0.01	1.36	9.27	2.93	0.70
I	192	1.85	2.12	0.14	1.42	8.89	3.20	0.83
S	200	1.85	0.58	< 0.01	0.97	9.02	2.25	0.66
V	192	2.00	< 0.01	< 0.01	9.87	5.63	5.50	0.71

RF: residual fraction, RSCbkg: ratio of background mean count with and without scatter correction

the number of updates generally decreased RF (Additional file 1) whereas RSCbkg was almost stable. For D, I and S, RF in the water insert levelled off at 100 updates without scatter correction.

Figure 2 shows 30-mm (height of the ROI used for CRC computation) thick transverse slices of TOM cold and hot inserts. Due to limited availability of the reconstruction computer, the NoSC images were not obtained for D. CRC in TOM for both ROI sizes are presented in Fig. 3 for cold rods and in Fig. 4 for hot rods with and without scatter correction. CRC increased with update number for both cold and hot rods. SC and NoSC COV of TOM uniform parts are plotted against update number in Fig. 5. For all four systems, COV increased with number of updates and was always lower without scatter correction. The results when additionally using PSFRq with V are also presented in Figs. 3, 4, 5.

For quantification, only SC data were considered. Results are presented at 192 or 200 updates for the various ROI sizes and both L and XL calibration phantoms in Table 2 for NEMA and in Table 3 for TOM. For TOM (Additional files 2 and 3), the quantification error increased very moderately up to about 100 updates and became mostly stable above this. For NEMA (Additional files 4 and 5), a moderate decrease was observed when increasing the number of iterations for all systems except I, where the decrease was more pronounced. Between 200 and 240 updates, a very sharp increase (ΔA increased roughly by 15) was observed for S and NEMA. Table 4 presents the quantification error in L using XL as calibration phantom for all ROI drawn in both phantoms. The uniformity of the slices for the two uniform phantoms can be visually evaluated from Additional files 6 and 7.

Finally, Table 5 reports the normalised acquisition durations for the four phantoms. The XL phantom imaged with the conventional I system was arbitrarily taken as the reference.

Discussion

The present study used the experimental design of our previous study [23]. The fundamentals of this design were, as much as possible, to use the default manufacturer-recommended acquisition and reconstruction parameters while reaching the highest possible standardisation between the systems for objective comparison. Particular attention was paid to obtaining an almost identical pixel size, number of steps for rotating systems, focus mode and rotation number for ring systems, total number of counts and OSEM updates. Default manufacturer-defined parameters were used for energy windows,

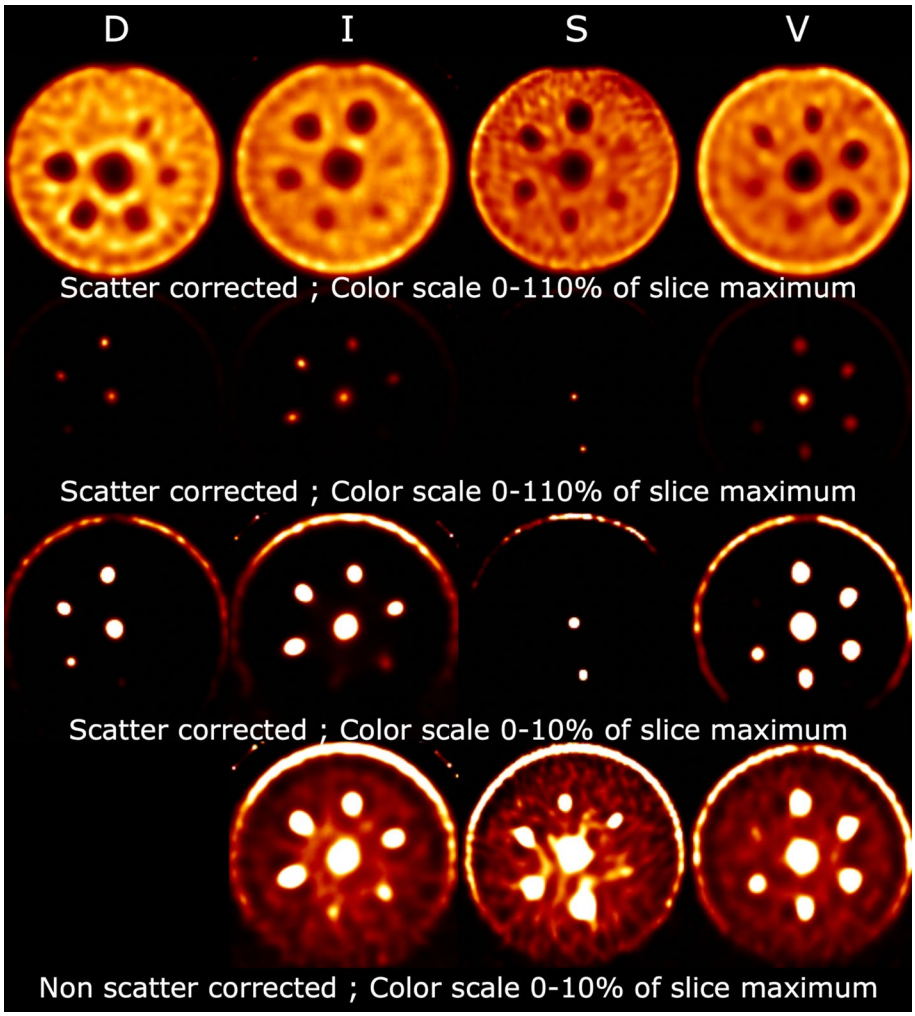

Fig. 2 30-mm thick transverse slice of the cold (first row) and hot (second to fourth rows) rod parts of the contrast phantom for the four SPECT-CT systems after 192 (I,V) or 200 (D,S) updates with attenuation correction and resolution recovery.

number of subsets, AC, SC and RR correction methods. This seemed essential particularly for CZT-based systems for which the overall knowledge is far more limited than for a NaI dual-head camera. Moreover, the manufacturers of both ring CZT systems share very little information with the end-users. To our knowledge, the so-called wide-beam reconstruction [19] algorithm used by the manufacturer of the V system has not been fully described nor are their PSFRq and PSFRd additional resolution recovery methods. All this is regrettable and was recently pointed out as a remaining challenge on the road to quantification in SPECT [21]. We nevertheless found that for system S (and presumably D) the DEW method is applied at the level of the sinograms or projections whereas it is a post-reconstruction implementation for system V. The V software separately reconstructed the images of the photopeak window and the scatter window before making the weighted subtraction.

Another important point of our experiment design is the standardised preparation of the phantoms as described in the methods. Moreover, the activities in NEMA, TOM and

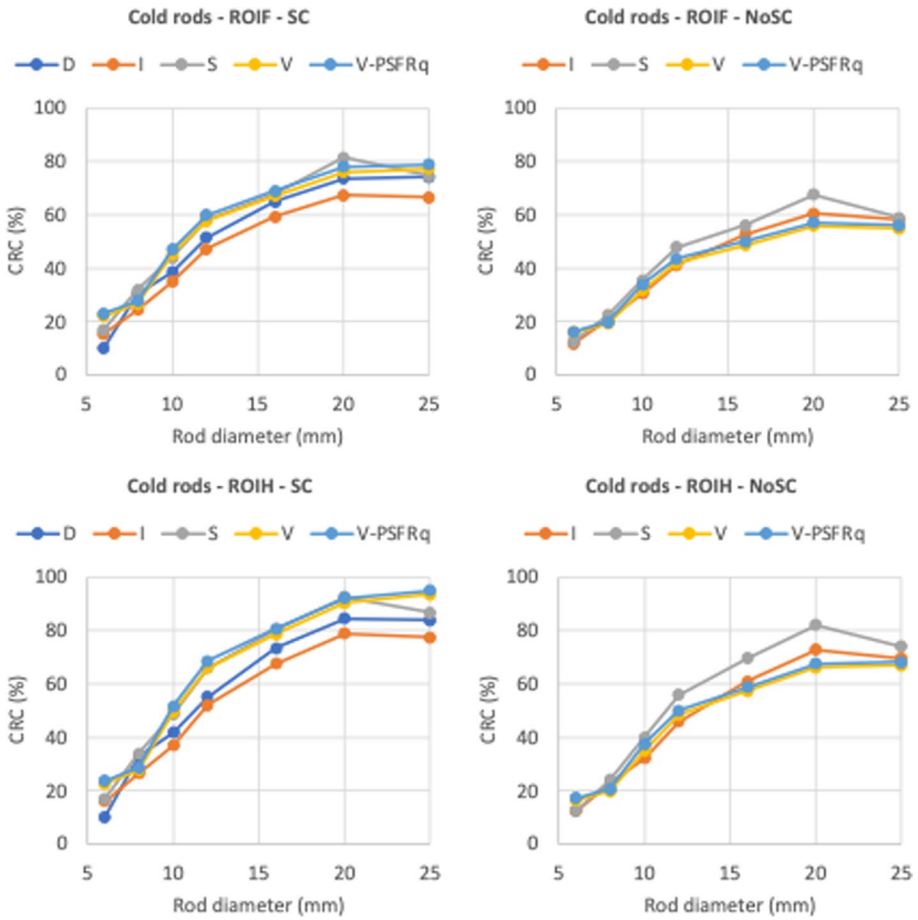

Fig. 3 Cold rod recovery coefficient in rod full (F) and half (H) physical diameter ROI with and without scatter correction at 192 (I,V) or 200 (D,S) updates. NoSC data were not available for D

XL were very similar, the activity in L being about 60% lower. This ensures that any possible activity measurement error due to the activimeter would be almost cancelled when computing ΔA, at least, when using the XL calibration factor.

The better energy resolution of CZT systems [2, 32] should lead to narrower energy windows compared to NaI systems [7, 30]. However, the manufacturer of D and S still advised the use of a classical 20%-wide photopeak energy window when SC is performed, and we followed this advice for these two systems. Moreover, marginal changes in CRC have been observed for D when decreasing the photopeak energy window width to 15% [1] or even down to a low 4% [30]. But, as pointed out by the authors of this last study, the systematic use of scatter correction could have masked the impact of the energy window narrowing. The correction methods are only partially described by the manufacturer and any user modification should be verified by extended experiment. This drove us to not only leave the correction parameters as factory-defined but also the energy windows.

A previous study [25] has shown possible dysfunction of some iterative algorithms when not using the default number of subsets. Therefore, only the number of OSEM iterations was varied to modify the number of updates. It was also decided to exclude

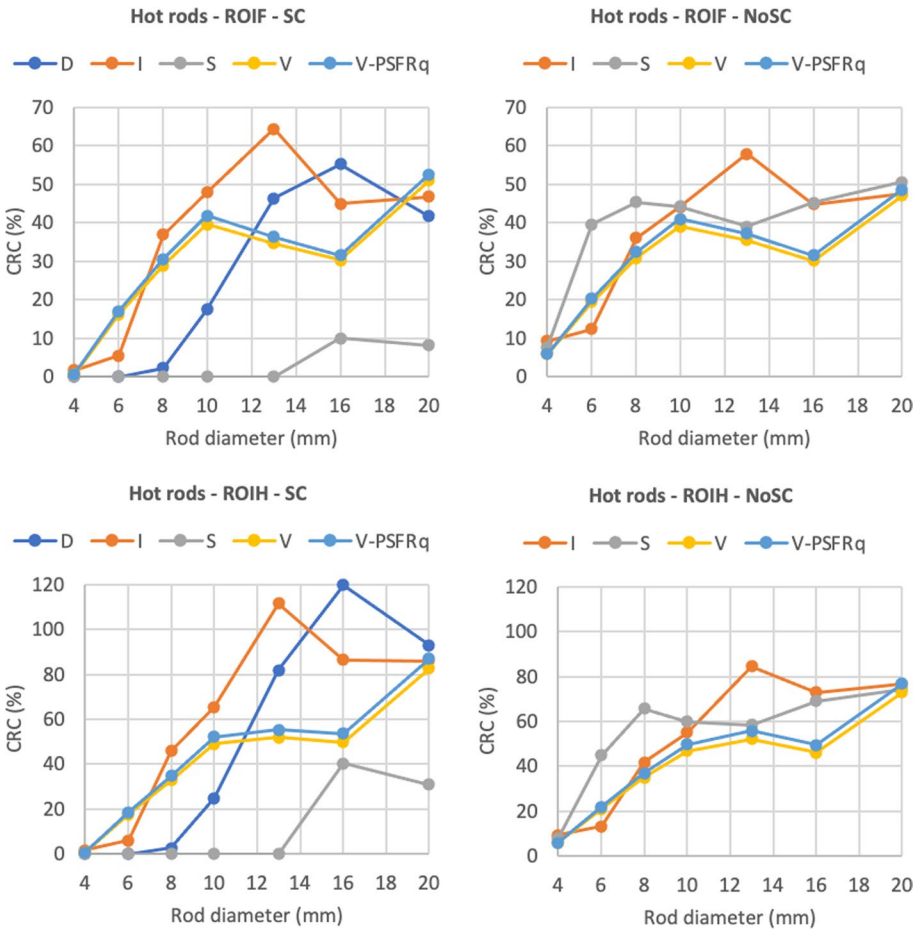

Fig. 4 Hot rod recovery coefficient in rod full (F) and half (H) physical diameter ROI with and without scatter correction at 192 (I,V) or 200 (D, S) updates. NoSC data were not available for D

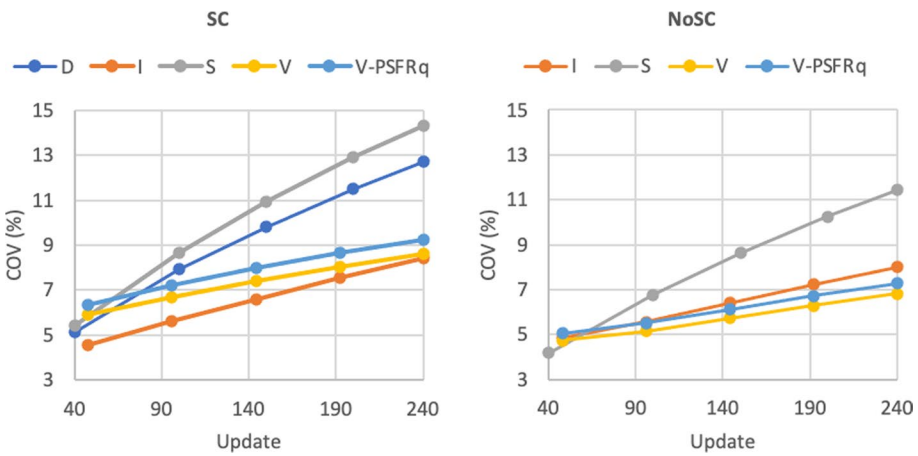

Fig. 5 Coefficient of variation in TOM uniform part with and without scatter correction. NoSC data were not available for D

Table 2 Quantification error in percent in NEMA phantom for various ROI sizes in calibration phantom images

Camera	Quantification error (%) at 192 (I, V) or 200 (D, S) updates										
	XL phantom ROI						L phantom ROI				
	−4	−2	0	2	4	Img	−2	0	2	4	Img
D	2.94	2.22	4.33	0.25	0.15	0.02	−5.09	7.06	1.12	0.77	−0.06
I	−2.77	−2.06	1.53	−0.99	−1.53	−1.67	−3.51	2.96	−1.89	−3.69	−3.69
S	5.59	3.36	3.61	2.60	2.60	2.60	0.02	3.24	1.55	1.45	1.04
V	−3.16	−5.07	−5.79	−8.44	−8.49	−8.49	n/a	n/a	n/a	n/a	n/a

Table 3 Quantification error in percent in TOM phantom for various ROI sizes in calibration phantoms

Camera	Quantification error (%) at 192 (I, V) or 200 (D, S) updates										
	XL phantom ROI						L phantom ROI				
	−4	−2	0	2	4	Img	−2	0	2	4	Img
D	8.16	7.4	9.62	5.33	5.22	5.09	−0.29	12.48	6.24	5.87	5.01
I	13.63	14.47	18.65	15.72	15.08	14.92	12.77	20.33	14.67	12.56	12.56
S	19.49	16.96	17.25	16.10	16.10	16.10	10.04	16.23	14.92	14.8	14.34
V	5.61	3.52	2.73	−0.15	−0.21	−0.32	n/a	n/a	n/a	n/a	n/a

Table 4 Quantification error in percent in L phantom using XL as calibration phantom for various ROI sizes in both phantoms

Camera	L phantom ROI	Quantification error (%) at 192 (I) or 200 (D, S) updates					
		XL phantom ROI					
		−4	−2	0	2	4	Img
D	−2	8.46	7.71	9.93	5.63	5.53	5.39
	0	−3.84	−4.51	−2.54	−6.35	−6.45	−6.57
	2	1.81	1.10	3.18	−0.85	−0.95	−1.08
	4	2.16	1.45	3.54	−0.51	−0.61	−0.74
	Img	3.00	2.28	4.39	0.31	0.21	0.08
I	−2	0.76	1.50	5.22	2.61	2.05	1.91
	0	−5.57	−4.88	−1.39	−3.83	−4.36	−4.49
	2	−0.90	−0.18	3.48	0.92	0.36	0.22
	4	0.94	1.69	5.41	2.80	2.23	2.09
	Img	0.94	1.69	5.41	2.80	2.23	2.09
S	−2	8.59	6.29	6.55	5.51	5.51	5.51
	0	2.28	0.11	0.35	−0.62	−0.62	−0.62
	2	3.98	1.78	2.03	1.03	1.03	1.03
	4	4.08	1.88	2.13	1.14	1.14	1.14
	Img	4.50	2.29	2.54	1.54	1.54	1.54
V		n/a	n/a	n/a	n/a	n/a	n/a

any post-filter. The selection of the filter kernel is task-dependent and should result from a local extended study [1, 31]. The use of an iterative algorithm with noise reduction was also discarded for similar reasons. These algorithms require systematic studies to define

Table 5 Relative duration of all acquisitions using XL phantom imaged with I system as reference

Phantom	Activity (MBq)	Total count number	Acquisition time (relative values)			
			D	I	S	V
L	300	85×10^6	1.20	1.11	0.77	0.43
XL	740	100×10^6	1.02	1.00	1.04	0.57
NEMA	740	100×10^6	0.89	0.85	0.89	0.45
TOM	740	100×10^6	1.02	1.03	0.99	0.52

the best trade-off for the clinical task between noise reduction and preservation of spatial resolution. Zorz et al. [7] explored such an algorithm with D and obtained lower CRC than with OSEM but increased contrast-to-noise ratio resulting from better noise control.

Very recently, Hoog et al. [2] proposed a head-to-head comparison of the ring systems S and V with a clinical oriented design (activity, acquisition time) and followed the manufacturer's advices for reconstruction. Among others, SC was performed with DEW for S and with PSFRq with V, whereas noise reduction was applied with V and not S. Our very high count study allowed us to not use noise reduction and we present the results obtained with and without scatter correction. As noted by Hoog et al. [2] a limitation of their study was the use of hot spheres (with a 10:1 sphere-to-background ratio) only. Both studies are complementary, with the present study being more raw performance oriented.

Throughout this discussion, it is also interesting to keep in mind that NaI camera I is an evolution of the camera from the same manufacturer explored in our previous study [23] and that the same Flash3D reconstruction algorithm was used in both studies. Gnesin et al. reported excellent quantitative results with ^{99m}Tc for the I system [14].

The RF values in NEMA with scatter correction (Table 1) were very low and very similar between the four systems while being systematically the lowest in water and Teflon inserts for the CZT systems. For the NaI camera, they were close to the results obtained in our previous study [23]. SC drastically reduced RF in water and Teflon (Table 1) whereas in air reduction or increase were observed but with a RF value remaining low. The RSCbkg (Table 1) of NaI-based system I was 0.83. For the three other systems and under the hypothesis that the difference in the reconstructed counts only resulted from the scatter correction, the scatter correction removed about 30% of the recorded counts in the NEMA phantom background for D and V and about 34% for S. Both manufacturers have kept a lot of details about their CZT ring system secret. It is therefore difficult to drawn any final conclusions on the differences in RSCbkg values from the partial information that they have shared with the end-users to date.

CRCcold increased with the rod diameter (Fig. 3) and the number of iterations, but levelled off above 20-mm rod diameter and at about 200 updates. CRCcold values were higher when SC was applied and the lowest for the NaI camera. CRCcold values were marginally increased by PSFRq (Fig. 3) or PSFRd (data not shown). Using similar acquisition conditions but a Chang-based attenuation and scatter correction, the cold rods of a Deluxe Jaszczak phantom were resolved down to 7.9 mm with S [7] whereas the limit seemed to lie between 7.9 and 9.5 mm with V [4]. In the same study, cold spheres

were clearly resolved in a Jaszczak phantom down to 12.7 mm diameter. Hoog et al. [2] obtained very comparable task transfer functions for S and V and concluded a similar spatial resolution for both systems with their acquisition and reconstruction conditions.

Overall CRChot also increased with rod diameter (Fig. 4) and number of updates but in a very system-dependent way. Irregular CRC versus hot sphere or rod diameter curves are very often observed when resolution recovery is applied and result from either the presence of one central peak of activity in small objects or two peaks at the border with one central valley in the larger objects. The phenomenon is present in positron emission tomography [31] and in SPECT [12]. It was observed in our previous study of NaI SPECT-CT [23] and was recently described for ring system S [5]. For most rods, the largest CRChot values were observed for the NaI camera but the dual-head CZT reached similar values for the three largest rods. For the CZT systems, SC improved CRChot for the largest rods while CRChot was reduced for the smallest, in perfect agreement with previous reports [1, 30]. While the rod insert was oriented differently between D and S systems, with the largest off-centre rod opposite to the bed for D and closest to the bed for S (Fig. 2), the smallest hot rods were absent from the scatter corrected images of both systems. The orientation of the insert in the phantom can therefore hardly be considered as the source of this absence. The two ring systems performed very differently but most of their CRChot values were much lower than for the two dual-head systems despite their much better SPECT spatial resolution [4, 7, 38]. S delivered the lowest CRChot and the thinnest hot rods were not visible on the images (Fig. 2). This clearly resulted from the SC as CRChot values were similar or even superior to those of the three other systems without SC (Fig. 4). The thinnest hot rods were also absent from the scatter corrected images provided by D system (Fig. 2). For V, CRChot values were not improved by SC or PSFRq. Both ring systems showed low SC performance for hot rods that led to suspected scatter over-correction. The scatter spectrum of CZT and NaI detectors are different [32]. Therefore, the SC strategies developed and validated for NaI detectors need to be revised when applied to a CZT detector [22], as well as the width of the photopeak window [32]. During this study, we were aware that the manufacturer of D and S had advised its customers to use a reduced photopeak window width for these CZT-based systems. It has been observed for NaI based systems that the TEW led to underestimation of activity in small spheres and overestimation in large hot spheres in a null background and that non-spectral techniques could be a better option for scatter correction [33]. Scatter overcorrection should lead to an artificially high CRCcold and low RF. Therefore, the observed lower water and Teflon RF (Table 1) and higher CRCcold values (Fig. 3) of CZT systems could result, at least partially, from incorrect SC.

Without scatter correction, CRChot values (Fig. 4) for V were lower than for the NaI or the most-similar S systems. This could result from the difference in collimator design. V uses a collimator that favours sensitivity, whereas S uses a longer bore collimator with lower sensitivity. PSFRq did not change CRChot values of V (Fig. 4), whereas they were largely increased by PSFRd with CRC values largely exceeding 100% in the central part of the largest rods (data not shown). For V, an abrupt increase of CRChot was observed for the largest rod (Fig. 4). In contrast to the other rods that are located off the cylinder axis, the largest rod is located on this axis. DEW scatter correction being applied or not, the results presented in Figs. 3 and 4 show almost no effect of PSFRq on hot and cold

contrasts. The same observation was found for RF in NEMA phantom. These results were contradictory to the claim that PSFRq offered a viable alternative to DEW for scatter correction [2]. PSFRd boosted CRC values, sometimes to values greatly exceeding 100%. Following the manufacturer's claim, PSFRd was developed for display purposes and should never be used for quantitative images.

The COV of the TOM uniform region increased with number of updates (Fig. 5) as could be anticipated from OSEM's well-known general behaviour. While SC barely changed the COV for the NaI system, it increased COV for the three CZT systems. At 200 iterations, SC COV were the lowest and almost identical for I and V. COV were about 50% higher for S than for the three other systems. For V, PSFRq added about 0.5% to COV values, while PSFRd almost doubled the COV values. An image structure difference between the outer part and the central part of the phantom transverse slices was noticed for S (Fig. 2 and Additional file 6), as also reported by Hoog et al. [2].

Quantification was based on calibration factors obtained using large uniform phantoms but also ROI of a size smaller, equal to or larger than the phantom physical size. On the basis of Monte Carlo simulations, the combination of a large uniform phantom with full image ROI was shown to be the best alternative to point source for calibration factor determination [34]. We also obtained better results with large phantoms in our past survey of NaI cameras [23]. However, in this previous study, only ROI smaller than the phantom were considered, and quantification appeared to be roughly independent of the ROI size. For both L and XL, the number of counts in ROI + 2 was 1 to 6% larger than in ROI0 and generally continued to slightly increase in ROI + 4 and ROIimg. Counts in the three largest ROI were consistently the lowest for system S with values not exceeding 2.2% of ROI0 counts. The existence of a few percent of counts at a large distance from the phantoms has been reported by others [35] and was also present in the images of our previous study [23], while not being described in detail at that time.

ΔA obtained with L and XL (Tables 2, 3, 4) calibration factors were in the same range for each phantom and each system. For NEMA (Table 2), the results were very positive for all four systems with absolute ΔA values below 10% and in several cases below 5%. This was also observed (Table 3) for TOM with D and V, whereas results for I and S were in the 10–20% range. For the NaI camera I, the quantification errors were in the same range for NEMA as in our previous study [23] but were worse for TOM. Others have reported an excellent ^{99m}Tc quantification capability (< 5%) for this system [14]. As I and V systems belong to the same department, the TOM and NEMA phantoms were prepared only once and scanned on both systems the same day. The results are therefore based on the same activity measurement. As a result of a data lost between acquisition and reconstruction, XL phantom was scanned twice with V. The recorded count rates per unit of activity were very similar. At this stage, we have no clear explanation for the less favourable results obtained for TOM with I and S. A quantification error of ± 5% was observed in a recent multi-centre study when using a large uniform phantom for calibration [36]. Values in Table 4 show similar results for quantification in uniform phantom L when using XL as calibration phantom. For system D, a good accuracy for thyroid uptake in phantoms and patients was recently reported [16] as well as a semi-quantification of DOPA transporter capability similar to what is obtained with NaI systems [37]. Vergnaud et al. [38] obtained excellent results for ^{177}LU-PSMA quantification

with V using a uniform phantom as calibration source. In their very recent investigation, Hoog et al. [2] reached the same conclusion and reported ^{99m}Tc quantification errors in the range 0.1–3.3% for both ring systems when using the manufacturer's calibration procedure.

The calibration factors cannot be used to compare system sensitivity as they are reconstruction algorithm dependent [2]. Acquisition times (Table 5) for the three large phantoms were comparable for D, I and S, and about 60% shorter for V. S took roughly 30% less time and V 60% to scan the smaller L phantom compared to the dual-head systems. This gain is directly linked to the smaller field of view needed for the smallest phantom and to the use of the focus mode [11] offered by these two systems. Different studies reported shorter acquisition times [3, 4, 39] or higher volumetric sensitivity [7] with ring systems than with a dual-head NaI SPECT camera, but the benefit was found to be object size-dependent. From the energy spectra, Hoog et al. [2] measured a 53% higher sensitivity for V compared to S. Results in Table 5 are in line with these studies but they cannot be directly compared due to the use of the focus mode in our study. These results also show a clear higher sensitivity for ring system V than for S. This difference can be related to the apparently shorter collimator bore length in V than in S [2].

Several limitations of this study remain. While ^{99m}Tc remains the emitter in most SPECT radiopharmaceuticals, other isotopes like ^{123}I, ^{131}I, ^{177}Lu or ^{188}Re, to name a few, are of growing interest [34]. It is not straightforward to extend our results to these multi-peak emitter isotopes without some experimental data. We have undertaken a detailed study of the energy window width with system S that we hope to finalise very soon. Our contrast phantom is made of hot rods in a cold background and this part of the phantom was sandwiched between two hot areas (cold insert and grid). Many scattered photons are likely to be emitted from the two areas and this could have had an impact on some of the results, especially the poor performance of SC with S system. We also plan to improve this phantom to avoid the free rotation of its contrast inserts. This would make it possible to keep the orientation of the various rods identical relative to the imaging bed of the investigated systems. Our results were obtained at clinical departments—the standard end-users of the systems—and with the software version that was available at the time of the experiments. Meanwhile, both manufacturers of CZT systems have been developing their scatter correction methods. Following information we obtained, SC would still be based on DEW but would now be performed in the iterative loop. Unfortunately, we could not determine whether energy tailing [22] is accounted for. There is no doubt that the manufacturers will continue in the forthcoming months and years to develop and to improve their CZT systems and that further phantom—and possibly patient comparative studies—with the various isotopes used in SPECT will be of great value.

Conclusions

CZT-based SPECT-CT without scatter correction demonstrated a contrast recovery for hot and cold small objects comparable to a state-of-the-art NaI-based system. However, the simple transposition of the spectral strategies developed for NaI cameras, namely dual energy windows or triple energy windows, initially used by the manufacturers for scatter correction with the CZT detectors appeared to possibly overcorrect. Notably, the

smallest hot rods were barely detectable or absent from the images of one of the ring CZT cameras. Nevertheless, using conversion factors directly determined by the end-user, quantification errors in the range of 10% or even 5% appeared to be possible. Both manufacturers of the studied ring CZT cameras continue to work on these systems. This should allow improved quantification and better contrast for small hot objects imaged with these disruptive SPECT systems.

Abbreviations

AC	Attenuation correction
Ames	Measured activity
Atrue	True activity
CF	Conversion factors
Ci	Mean number of counts in insert
Cbkg	Mean number of counts in background
Cbkg_NoSc	Mean number of counts in background without scatter correction
Cbkg_SC	Mean number of counts in background with scatter correction
COV	Coefficient of variation
CRC	Contrast recovery coefficient
CRCcold	Contrast recovery coefficient in a cold rod
CRChot	Contrast recovery coefficient in a hot rod
Crod	Mean number of counts in a rod region of interest
CT	X-ray computed tomography
Cunif	Mean number of counts in a uniform region
CZT	Cadmium zinc telluride
D	Discovery
DEW	Dual energy window
ΔA	Deviation in percent from the true activity (Atrue) or percent quantification error
I	Intevo
L	Uniform cylindrical phantom of medium size
NaI	Sodium iodide
NEMA	NU2-1994 attenuation and scatter correction accuracy phantom
NoSC	No scatter correction
OSEM	Ordered subset expectation maximisation
PSFRd	Point spread function recovery for display
PSFRq	Point spread function recovery for quantification
RF	Residual fraction
ROI	Region of interest
ROIF	Region of interest with full rod physical diameter
ROIimg	Region of interest encompassing the whole reconstructed image
ROIH	Region of interest with half rod physical diameter
ROI0	Cylindrical region of interest with a diameter equal to the physical diameter of the phantom
ROI-n	Cylindrical region of interest with a diameter n cm smaller than the physical diameter of the phantom
ROI + n	Cylindrical region of interest with a diameter n cm larger than the physical diameter of the phantom
RR	Resolution recovery
RSCbkg	Ratio of mean counts in the background with and without scatter correction
S	StarGuide
SC	Scatter correction
SDEV	Standard deviation
SPECT	Single-photon emission computed tomography
TEW	Triple energy window
TOM	Contrast phantom
V	Veriton
WB	Whole body
XL	Uniform cylindrical phantom of large size

Supplementary Information

The online version contains supplementary material available at https://doi.org/10.1186/s40658-025-00754-3.

Additional file 1.

Acknowledgements

The authors would like to thank the heads (at the time of the experiments) of the nuclear medicine departments of CHU Liège, CHR Citadelle and Vivalia-Hôpital de Libramont for providing access to the various cameras used in this work. We are truly grateful to the reviewers whose detailed and critical reading and very constructive remarks have undoubtedly

led to improvements of this report. In particular, we thank the reviewer that brought to us the information about a private DICOM tag used by manufacturer of system I.

Author contributions
AS designed the experiments, participated in data acquisition, analysed the images and drafted the manuscript. CB performed all acquisitions, participated in the image analysis and manuscript writing. Both authors read and approved the final manuscript.

Funding
Not applicable.

Availability of data and materials
The datasets used and/or analysed during the current study are available from the corresponding author on reasonable request.

Declarations

Ethics approval and consent to participate
Not applicable.

Consent for publication
Not applicable.

Competing interests
The authors declare that they have no competing interests.

Received: 25 November 2024 Accepted: 18 April 2025
Published online: 10 May 2025

References

1. Zhang R, Wang M, Zhou Y, Wang S, Shen Y, Li N, et al. Impacts of acquisition and reconstruction parameters on the absolute technetium quantification of the cadmium–zinc–telluride-based SPECT/CT system: a phantom study. EJNMMI Phys. 2021;8:66. https://doi.org/10.1186/s40658-021-00412-4.
2. Hoog C, Koulibaly P-M, Sas N, Imbert L, Le Rouzic G, Popoff R, et al. 360° CZT-SPECT/CT cameras: ^{99m}Tc- and ^{177}Lu-phantom-based evaluation under clinical conditions. EJNMMI Phys. 2024;11:89. https://doi.org/10.1186/s40658-024-00684-6.
3. Cassol E, Gantet P, Payoux P. Veriton system: quantitative evaluation based on Jaszczak and striatal phantom. Med Nucl. 2019;43:237–40.
4. Desmonts C, Bouthiba MA, Enilorac B, Nganoa C, Agostini D, Aide N. Evaluation of a new multipurpose whole-body CZT-based camera: comparison with a dual-head Anger camera and first clinical images. EJNMMI Phys. 2020;7:18. https://doi.org/10.1186/s40658-020-0284-5.
5. Danieli R, Stella M, Leube J, Tran-Gia J, Marin C, Uribe CF, et al. Quantitative ^{177}Lu SPECT/CT imaging for personalized dosimetry using a ring-shaped CZT-based camera. EJNMMI Phys. 2023;10:64. https://doi.org/10.1186/s40658-023-00586-z.
6. Bailly M, Callaud A, Metrard G. Dynamic cardiac SPECT with flow measurement using 3D-ring CZT: when SPECT is inspired by PET. Eur J Nucl Med Mol Imaging. 2023;50:1837–9. https://doi.org/10.1007/s00259-022-06106-y.
7. Zorz A, Rossato MA, Turco P, Colombo Gomez LM, Bettinelli A, De Monte F, et al. Performance evaluation of the 3D-ring cadmium–zinc–telluride (CZT) StarGuide system according to the NEMA NU 1–2018 standard. EJNMMI Phys. 2024;11:69. https://doi.org/10.1186/s40658-024-00671-x.
8. Birnbacher L, Braig E-M, Pfeiffer D, Pfeiffer F, Herzen J. Quantitative X-ray phase contrast computed tomography with grating interferometry: biomedical applications of quantitative X-ray grating-based phase contrast computed tomography. Eur J Nucl Med Mol Imaging. 2021;48:4171–88. https://doi.org/10.1007/s00259-021-05259-6.
9. Bailey DL, Willowson KP. An evidence-based review of quantitative SPECT imaging and potential clinical applications. J Nucl Med. 2013;54:83–9. https://doi.org/10.2967/jnumed.112.111476.
10. Dickson JC, Armstrong IS, Minguez Gabiña P, Denis-Bacelar AM, Krizsan AK, Gear JM, et al. EANM practice guideline for quantitative SPECT-CT. Eur J Nucl Med Mol Imaging. 2023;50:980–95. https://doi.org/10.1007/s00259-022-06028-9.
11. Graham R, Morland D, Cade S, Imbert L, Panagiotidis E, Kurth J, et al. EANM position paper on challenges and opportunities of full-ring 360° CZT bone imaging: it's time to let go of planar whole-body bone imaging. Eur J Nucl Med Mol Imaging. 2025;52:1200–9. https://doi.org/10.1007/s00259-024-06906-4.
12. Peters SMB, van der Werf NR, Segbers M, van Velden FHP, Wierts R, Blokland KAK, et al. Towards standardization of absolute SPECT/CT quantification: a multi-center and multi- vendor phantom study. EJNMMI Physics. 2019;6:29. https://doi.org/10.1186/s40658-019-0268-5.
13. Da Silva AJ, Tang HR, Wong KH, Wu MC, Dae MW, Hasegawa BH. Absolute quantification of regional myocardial uptake of 99mTc-sestamibi with SPECT: experimental validation in a porcine model. J Nucl Med. 2001;42:772–9.
14. Gnesin S, Ferreira PL, Malterre J, Laub P, Prior JO, Verdun FR. Phantom validation of Tc-99m absolute quantification in a SPECT/CT commercial device. Comput Math Methods Med. 2016;2016:4360371. https://doi.org/10.1155/2016/4360371.

15. Lee WW. Clinical applications of technetium-99m quantitative single-photon emission computed tomography/computed tomography. Nucl Med Mol Imaging. 2019;53:172–81. https://doi.org/10.1007/s13139-019-00588-9.
16. Serrano B, Amblard R, Beaumont T, Hugonnet F, Dietz M, Berthier F, et al. Quantitative analysis of ^{99m}Tc-pertechnetate thyroid uptake with a large-field CZT gamma camera: feasibility and comparison between SPECT/CT and planar acquisitions. EJNMMI Phys. 2023;10:45. https://doi.org/10.1186/s40658-023-00566-3.
17. Yamane T, Kuji I, Seto A, Matsunari I. Quantification of osteoblastic activity in epiphyseal growth plates by quantitative bone SPECT/CT. Skeletal Radiol. 2018;47:805–10.
18. Vargas CS, Pérez SR, Baete K, Pommé S, Paepen J, Van Ammeld R, et al. Intercomparison of ^{99m}Tc, ^{18}F and ^{111}In activity measurements with radionuclide calibrators in Belgian hospitals. Physica Med. 2018;45:134–42. https://doi.org/10.1016/j.ejmp.2017.12.011.
19. Borges-Neto S, Pagnanelli RA, Shaw LK, Honeycutt E, Shwartz SC, Adams GL, et al. Clinical results of a novel wide beam reconstruction method for shortening scan time of Tc-99m cardiac SPECT perfusion studies. J Nucl Cardiol. 2007;14:555–65. https://doi.org/10.1016/j.nuclcard.2007.04.022.
20. Zeintl J, Vija HA, Yahil A, Hornegger J, Kuwert T. Quantitative accuracy of clinical ^{99m}Tc SPECT/CT using ordered-subset expectation maximization with 3-dimensional resolution recovery, attenuation, and scatter correction. J Nuc Med. 2010;51:921–8. https://doi.org/10.2967/jnumed.109.071571.
21. Van den Wyngaert T, Elvas F, De Schepper S, Kennedy JA, Israel O. SPECT/CT: standing on the shoulders of giants, it is time to reach for the sky! J Nucl Med. 2020;61:1284–91. https://doi.org/10.2967/jnumed.119.236943.
22. Pourmoghaddas A, Vanderwerf K, Ruddy TD, Wells RG. Scatter correction improves concordance in SPECT MPI with a dedicated cardiac SPECT solid-state camera. J Nucl Cardiol. 2015;22:334–43. https://doi.org/10.1007/s12350-014-0008-0.
23. Seret A, Nguyen D, Bernard C. Quantitative capabilities of four state-of-the-art SPECT-CT cameras. EJNMMI Res. 2012;2:45; http://www.ejnmmires.com/content/2/1/45.
24. National Electrical Manufacturers Association (NEMA). Performance measurements of positron emission tomographs, NEMA standards publication NU2. Washington, DC: NEMA; 1994.
25. Seret A, Forthomme J. A comparison of different types of commercial FBP and OSEM SPECT reconstruction software. J Nucl Med Technol. 2009;37:179–87. https://doi.org/10.2967/jnmt.108.061275.
26. Jaszczak RJ, Floyd CE, Coleman RE. Scatter compensation techniques for SPECT. IEEE Trans Nucl Sci. 1985;32:786–93.
27. Ogawa K, Harata Y, Ichihara T, Kubo A, Hashimoto S. A practical method for position-dependent Compton scatter compensation in single photon emission CT. IEEE Trans Med Imaging. 1991;10:408–12.
28. Ichihara T, Ogawa K, Motomura N, Kubo A, Hashimoto S. Compton scatter compensation using the triple-energy window method for single- and dual- isotope SPECT. J Nucl Med. 1993;34:2216–21.
29. Carnegie-Peak L, Taprogge J, Murray I, Flux GD, Gea J. Quantification and dosimetry of small volumes including associated uncertainty estimation. EJNMMI Phys. 2022;9:86. https://doi.org/10.1186/s40658-022-00512-9.
30. Arvola S, Seppänen S, Timonen KL, Rautio P, Ettala O, Anttinen M, et al. Detection of prostate cancer bone metastases with fast whole-body ^{99m}Tc-HMDP SPECT/CT using a general-purpose CZT system. EJNMMI Phys. 2022;9:85. https://doi.org/10.1186/s40658-022-00517-4.
31. Munk OL, Tolbod LP, Hansen SB, Bogsrud TV. Point-spread function reconstructed PET images of sub-centimeter lesions are not quantitative. EJNMMI Phys. 2017;4:5. https://doi.org/10.1186/s40658-016-0169-9.
32. Ito T, Matsusaka Y, Onoguchi M, Ichikawa H, Okuda K, Shibutani T, et al. Experimental evaluation of the GE NM/CT 870 CZT clinical SPECT system equipped with WEHR and MEHRS collimator. J App Clin Med Phys. 2021;22:165–77. https://doi.org/10.1002/acm2.13158.
33. Uribe CF, Esquinas PL, Tanguay J, Gonzalez M, Gaudin E, Beauregard J-M, et al. Accuracy of ^{177}Lu activity quantification in SPECT imaging: a phantom study. EJNMMI Phys. 2017;4:2. https://doi.org/10.1186/s40658-016-0170-3.
34. Zhao W, Esquinas PL, Hou X, Uribe CF, Gonzalez M, Beauregard J-M, et al. Determination of gamma camera calibration factors for quantitation of therapeutic radioisotopes. EJNMMI Phys. 2018;5:8. https://doi.org/10.1186/s40658-018-0208-9.
35. Frezza A, Desport C, Uribe C, Zhao W, Celler A, Després P, et al. Comprehensive SPECT/CT system characterization and calibration for ^{177}Lu quantitative SPECT (QSPECT) with dead-time correction. EJNMMI Phys. 2020;7:10. https://doi.org/10.1186/s40658-020-0275-6.
36. Okuda K, Hasegawa D, Kamiya T, Ichikawa H, Umeda T, Ohkubo T, et al. Multicenter study of quantitative SPECT: reproducibility of ^{99m}Tc quantitation using a conjugated-gradient minimization reconstruction algorithm. J Nucl Med Technol. 2021;49:138–42. https://doi.org/10.2967/jnmt.120.256131.
37. Thiele F, Schau F, Rogasch JMM, Wetz C, Bluemel S, Brenner W, et al. Same same but different: dopamine transporter SPECT on scanners with CZT vs. NaI detectors. EJNMMI Res. 2023;13:24. https://doi.org/10.1186/s13550-023-00973-8.
38. Vergnaud L, Badel J-N, Giraudet A-L, Kryza D, Mognetti T, Baudier T, et al. Performance study of a 360° CZT camera for monitoring ^{77}Lu-PSMA treatment. EJNMMI Phys. 2023;10:58. https://doi.org/10.1186/s40658-023-00576-1.
39. Song H, Ferri V, Duan H, Aparici CM, Davidzon G, Franc BL, et al. SPECT at the speed of PET: a feasibility study of CZT-based whole-body SPECT/CT in the post ^{177}Lu-DOTATATE and ^{177}Lu-PSMA617 setting. Eur J Nucl Med Mol Imaging. 2023;50:2250–7. https://doi.org/10.1007/s00259-023-06176-6.

Publisher's Note